

MATERIALS SCIENCE

Giant tuning of ferroelectricity in single crystals by thickness engineering

Zibin Chen^{1*†}, Fei Li^{2*}, Qianwei Huang¹, Fei Liu³, Feifei Wang³, Simon P. Ringer¹, Haosu Luo⁴, Shujun Zhang^{5†}, Long-Qing Chen⁶, Xiaozhou Liao^{1†}

Thickness effect and mechanical tuning behavior such as strain engineering in thin-film ferroelectrics have been extensively studied and widely used to tailor the ferroelectric properties. However, this is never the case in free-standing single crystals, and conclusions from thin films cannot be duplicated because of the differences in the nature and boundary conditions of the thin-film and freestanding single-crystal ferroelectrics. Here, using in situ biasing transmission electron microscopy, we studied the thickness-dependent domain switching behavior and predicted the trend of ferroelectricity in nanoscale materials induced by surface strain. We discovered that sample thickness plays a critical role in tailoring the domain switching behavior and ferroelectric properties of single-crystal ferroelectrics, arising from the huge surface strain and the resulting surface reconstruction. Our results provide important insights in tuning polarization/domain of single-crystal ferroelectric via sample thickness engineering.

INTRODUCTION

The successful fabrication of relaxor-PbTiO₃ (PT)-based ferroelectric single crystals in the 1980s (1, 2), such as Pb(Zn_{1/3}Nb_{2/3})O₃-PbTiO₃ (PZN-PT) and Pb(Mg_{1/3}Nb_{2/3})O₃-PbTiO₃ (PMN-PT), is considered an important milestone in the piezoelectric research field. These crystals have ultrahigh piezoelectric coefficients d_{33} of >1500 pC/N, which are far superior to those of conventional ferroelectric ceramics [e.g., Pb(Zr, Ti)O₃] (3). This has been the driving force for emerging applications of high-performance piezoelectric sensors and transducers (4–11), where the high piezoelectric and electromechanical properties are demanded. The high piezoelectric properties of relaxor-PT single crystals can be successfully explained by the engineered domain configurations (12) and the existence of collinear polar nanoregions that facilitate macroscopic polarization rotation (13). On the basis of these concepts, extremely high d_{33} of ~3400 to 4100 pC/N has been achieved in Sm³⁺-doped PMN-PT crystals (14). In addition to the piezoelectric properties, ferroelectric domain switching behavior under electric field is also important in ferroelectric materials, which has been at the center stage and extensively studied (15, 16).

Many approaches have been proposed to tailor the ferroelectric domain switching behavior, where the application of external stress/strain confinement was confirmed to be an effective way to facilitate the domain switching and thus modify the ferroelectricity in thin films (17, 18). Regardless of the improvement in ferroelectricity, the way to provide external strain field will lead to an extra energy consumption that is not practically desirable. On the contrary, intrinsic

strain manipulation is found to be an ideal solution for tailoring the ferroelectricity of thin-film materials by changing their thickness (structural tuning) (19, 20), where the interfacial constraint, induced by the lattice mismatch or thermal expansion difference between a film and its substrate, is expected to modify the structural parameters including lattice parameters and the strain, thus substantially altering the ferroelectricity (21). It was observed that ferroelectricity still exists in 1.5 unit cell of thin films due to the help of the substrate/film interface to persist the polarization order in the thin-film ferroelectric (19). The film/substrate interface clamping energy is so large that even a small change in film thickness can markedly alter the properties. However, this is never the case in freestanding single crystals because of the lack of a strained interface. For a long time, a freestanding single crystal is expected to relax in all directions, which is insensitive to thickness.

With the fast growth of internet of things, millions of micro/nano-electromechanical systems (MEMS/NEMS) are in demand. In this scenario, the thin-film ferroelectric has its own advantages because of its excellent ferroelectric behavior, controllable film thickness, and the possibility that the ferroelectricity can be tuned by film thickness and substrate. Single-crystal ferroelectrics, however, have shown much better fatigue behavior because of the stand-free condition and much improved crystallinity (a thin film crystallizes at about 600° to 700°C, while a single crystal is grown directly from melt at above 1280°C) compared with thin films (14, 22). Furthermore, single-crystal ferroelectrics can be easily integrated on silicon substrate on modern devices by lithography methods (23) without the clamping effect from the substrate, which is advantageous for memory device applications. However, it is extremely difficult to measure or tune the ferroelectricity on the nanometer scale for single crystals. Nevertheless, the size-dependent phenomena and relevant ferroelectric domain switching dynamics have not been investigated, which is critical for designing ferroelectric NEMS/MEMS and nonvolatile ferroelectric memory devices. Therefore, it is desired to explore the impact of sample thickness on ferroelectricity and the underlying mechanism controlling the properties in nanoscale single-crystal ferroelectrics.

Ferroelectric surfaces that have a broken symmetry layer with thickness down to the nanometer size affect the nearby structure substantially (24). Recent studies suggested that the polarization of

Copyright © 2020
The Authors, some
rights reserved;
exclusive licensee
American Association
for the Advancement
of Science. No claim to
original U.S. Government
Works. Distributed
under a Creative
Commons Attribution
NonCommercial
License 4.0 (CC BY-NC).

¹School of Aerospace, Mechanical and Mechatronic Engineering, The University of Sydney, Sydney, NSW 2006, Australia. ²Electronic Materials Research Laboratory, Key Laboratory of the Ministry of Education, Xi'an Jiaotong University, Xi'an 710049, China. ³Key Laboratory of Optoelectronic Material and Device, Department of Physics, Shanghai Normal University, Shanghai 200234, China. ⁴Key Laboratory of Inorganic Functional Materials and Devices, Shanghai Institute of Ceramics, Chinese Academy of Sciences, Shanghai 201899, China. ⁵Institute for Superconducting and Electronic Materials, Australian Institute of Innovative Materials, University of Wollongong, Wollongong, NSW 2522, Australia. ⁶Materials Research Institute, Department of Materials Science and Engineering, The Pennsylvania State University, University Park, PA 16802, USA.

*These authors contributed equally to this work.

†Corresponding author. Email: z.chen@sydney.edu.au (Z.C.); shujun@uow.edu.au (S.Z.); xiaozhou.liao@sydney.edu.au (X.L.)

the surface of ferroelectric materials was different than that underneath, forming a reconstructed surface layer that could alter the physical and chemical properties (25) of the materials. The bound charges and lattice distortion from the reconstructive surface could dramatically affect internal polarization rotation (5, 17). Thus, the combination of the surface energy (26), domain wall energy (27, 28), structural defects (29, 30), and/or surface chemical variation (31) has great potential to tailor the ferroelectricity, especially when a material has a large specific surface (17). The ferroelectric properties of a nanometer-scale single-crystal ferroelectric can therefore be affected by such internal factor where the reconstructed surface layer becomes more important, thus greatly affecting the rotation and/or switching of polarization. Thanks to the development of modern in situ electron microscopy, the unmeasurable piezoelectric responses in nanoscale samples that have large surface volume ratios can now be captured through imaging the dynamic polarization rotation processes (32–34). With the help of the state-of-art aberration-corrected (scanning) transmission electron microscopy [(S)TEM] that provides information on atomic displacements in the sample surface region, it is now possible to explore the in situ polarization rotation behavior.

Here, we used in situ biasing TEM and aberration-corrected STEM to study the thickness dependence of polarization rotation behavior in $\text{Pb}(\text{Mg}_{1/3}\text{Nb}_{2/3})\text{O}_3$ -38% PbTiO_3 (PMN-38%PT) single crystals with submicrometer to nanoscale thicknesses. We discovered that the domain switching behavior is substantially affected by the sample thickness. There is a reconstructed randomly polarized surface layer with a thickness of ~ 30 atomic columns (~ 4.5 nm), which produces a local strain field that prohibits domain switching/polarization rotation across domain walls. This effect is greatly weakened by decreasing the surface volume ratio, revealing that the ferroelectricity can be substantially tailored by varying the sample thickness. These results open a new door for structurally tuning the ferroelectricity in single-crystalline ferroelectrics.

RESULTS

Figure 1A presents the schematic setup of the in situ biasing experiments of electron transparent PMN-38%PT samples to reveal the sample thickness effect on the ferroelectric domain switching at the nanoscale. The crystallographic orientation of the samples is also shown in Fig. 1A: [100] was parallel to the sample width. [010] was opposite to the electron beam direction and along the thickness direction. [001] was along the sample length and parallel to the biasing direction. The three samples used in this study were made from a large single crystal and marked with 1, 2, and 3 in Fig. 1A, with the same dimension of $20 \mu\text{m}$ by $2 \mu\text{m}$ by $1 \mu\text{m}$ (length by width by thickness). They are fixed on a copper platform using platinum deposition. A thin “window” was prepared in the middle of each of the dumbbell-shaped sample with a dimension of length of $3 \mu\text{m}$ and width of $2 \mu\text{m}$ and varying thickness of 170 nm (sample 1), 50 nm (sample 2), and 50 nm (sample 3), ensuring that the sample thickness was the only variable in the experiments. More samples with different thicknesses have also been examined. The results of the samples with thicknesses of 120 nm (sample S1) are given in section S8. A sample with thickness of 70 nm in the center and 100 nm in the outer area (sample S3) is also given in section S9. In situ electrical loading was applied by a conductive probe in TEM. The copper platform and the conductive probe served as the two electrodes. A

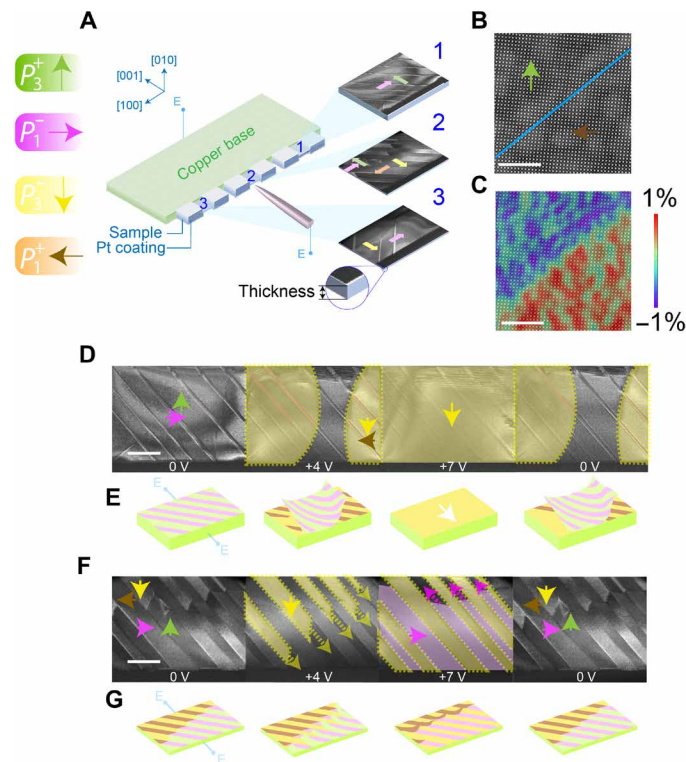


Fig. 1. In situ TEM setup and domain configurations and the thickness dependence of ferroelectric/ferroelastic domain switching under electric biasing.

(A) Schematic diagram of the experimental setup. Samples marked “1,” “2,” and “3” were of thicknesses of 170, 50, and 50 nm, respectively. A dark-field TEM image of the three samples represents their initial domain configurations. Head-to-tail tetragonal domains with their polarization directions are marked using colored vectors. (B) A STEM-HAADF image showing a typical 90° ferroelastic domain. Scale bar, 2 nm. (C) STEM-HAADF image overlaid with strain color map (strain tensor ϵ_{xx} , the magnitude ranges from -1 to 1%) determined by geometric phase analysis. The ϵ_{xx} component represents the field strains for in-plane direction. Scale bar, 2 nm. (D) A series of images showing the evolution of ferroelectric/ferroelastic domains in the thick sample (sample 1) with increasing bias and after the bias was withdrawn. Colored arrows represent local polarization directions. The switched domain areas are marked by brown/yellow colors, while the newly formed domain boundaries are marked by dashed lines. Diffraction patterns were taken for sample 1 at 0 and +10 V to confirm the domain orientation (see section S2 for detailed information). Scale bar, 500 nm. (E) Schematic diagrams of the domain evolution behavior in (D). The domain evolution exhibited the crossing mode. (F) A series of images showing the evolution of ferroelectric/ferroelastic domain switching behavior in a thin sample (sample 2) with increasing bias and after the bias was withdrawn. The switched domain areas are marked by yellow/purple colors, while the newly formed domain boundaries are marked by dashed lines. The domain switching directions are marked by dashed arrows in different colors. Scale bar, 500 nm. (G) Schematic drawing of the domain evolution behavior in (F). The domain evolution exhibits the directional mode.

thin layer of platinum was deposited at the front end of each sample to ensure uniform electrical loading through each sample. It is confirmed from the experiment presented in section S10 that platinum electric contact does not affect domain switching dynamic. Lamellar-like 90° ferroelastic domains (polarization directions are indicated by colored arrows) were observed in all three samples, in which the polarization was determined using electron diffraction and atomic-resolution high-angle annular dark-field (HAADF) imaging (details of the polarization determination are available in sections S1 to S4).

Throughout the paper, tetragonal domains with polarization along the positive and negative [100], [010], and [001] axes are referred to as $P_1^{+/-}$, $P_2^{+/-}$, and $P_3^{+/-}$, respectively. Figure 1B highlights a typical 90° ferroelastic domain boundary in an HAADF image. It can be seen clearly that large strains exist between both sides of the boundary, as evidenced by geometric phase analysis as shown in Fig. 1C.

Both samples 1 and 2 have P_3^+/P_1^- domain structures at the initial stage that allow direct comparison of the thickness effect. To capture the evolution of the domain configuration with different thicknesses, in situ experiments with ramping electrical bias from 0 to +10 V along the [00T] direction were conducted as shown in Fig. 1D. Snapshot images extracted from movies S1 and S2 are presented in Fig. 1 (D and F) and schematically illustrated in Fig. 1 (E and G), respectively. The initial domain configuration of sample 1 with alternative P_3^+/P_1^- domains (denoted by green and purple arrows, respectively) is shown in Fig. 1D. No domain switching took place until +2 V, as the electric field was still below the coercive field and therefore did not trigger domain reorientation. Upon increasing the electrical bias, domain propagation occurred in an unexpectedly fast manner. Two-thirds of the domains reoriented when the bias reached +4 V. Colors are used to highlight the reoriented domain region with different polarization directions, where the newly formed domain walls are denoted by dashed lines. Three types of polarization rotations were observed: (I) direct rotation from P_3^+ to P_3^- (green-to-yellow conversion), (II) direct rotation from P_1^- to P_1^+ (pink-to-brown conversion), and (III) P_1^- to P_3^- rotation (pink-to-yellow conversion). Types I and II were direct 180° ferroelectric switching, in which the P_3^+ to P_3^- rotation occurred simultaneously with the P_1^- to P_1^+ rotation to minimize the electrostatic force and neutralize bound charges along domain walls. Type III, however, was a combination of 180° ferroelectric switching P_1^- to P_1^+ and 90° ferroelastic switching P_1^- to P_3^- , which was associated with a considerable amount of strain. The propagation of the type III switching across all the initial 90° domain walls forms two curved domain walls against the unchanged domains, as marked by the brown dashed lines. Along the curved domain walls, all 180° P_3^+/P_3^- domain walls, 180° P_1^-/P_1^+ domain walls, and 90° P_1^-/P_3^- domain walls were identified. Of particular interest is that all domains merged when the electrical bias reached +7 V, forming a single domain with the P_3^- alignment along the applied electric field. Although a single domain was formed, residual contrast of the domain walls still exists. This is believed to be caused by the high strain field between the surface/domain wall, which will be explained in the following section. After removing the bias, partial domain reversal took place, leaving behind two newly formed domain boundaries marked by yellow dashed lines. Figure 1E schematically shows the domain evolution process. The domain reversal in the thick sample passes across all domain walls and triggers both 180° and 90° domain reorientations. For the convenience of future discussion, we use the “crossing mode” to describe this type of domain evolution in thick samples (type I).

Compared with sample 1 with a large thickness, sample 2 with a much thinner thickness shows a completely different domain evolution process. Four types of domains were observed and found joining into a quad point. With increasing electric bias, P_3^+/P_3^- domain walls started to move along the [T0T] direction (as marked by green dashed arrows). The moving direction of the domain walls remained parallel to the 90° P_3^+/P_1^- domain walls in the entire experiment. In contrast to the domain evolution in sample 1, the domain evolution process in sample 2 took place by steps. P_3^+ -to- P_3^- rotation

was the only domain switching that occurred before the bias of +4 V, as shown in the yellow regions. Because of the polarization rotation from P_3^+ to P_3^- , charged P_3^-/P_1^- domain walls were left behind. Accompanying the continued motion of the P_3^+/P_3^- domain walls, the P_1^-/P_1^+ domain walls started moving along the opposite direction, i.e., the [101] direction (as marked by purple dashed arrows), as shown in the snapshot image with bias of +7 V. Despite the expansion of charge domain walls, no domain merge was observed, indicating the undestroyable feature of the 90° ferroelastic domain walls in thin samples. Unlike sample 1, domain morphology in the thin sample (sample 2) fully returned to the original morphology, showing a complete domain reversal behavior, as shown in the image when the bias was removed. This indicates that much higher remanent polarization exists in the thick sample. The domain evolution process in sample 2 is schematically shown in Fig. 1G. The domain switching occurs along the direction parallel to the initial 90° ferroelastic domain walls. This directional domain switching behavior in thin samples (type II) is thereafter called the “directional mode.”

The crossing mode and the directional mode in samples 1 and 2, respectively, illuminate how polarization rotation or domain switching responds to the electric field on different thickness scales. Note that domain width in the sample does not affect the domain switching dynamic, as shown in section S8. The sample with gradient thickness of 70 nm in the center and 100 nm in the outer area (section S9) shows coexisting directional and crossing modes in the same sample. No other mode was found in thickness between 50 and 170 nm. The result of sample S3 in section S9 reveals there is a critical thickness that the polarization rotation mode switches from the crossing mode to directional mode. The crossing mode is dominated with the thickness above the critical value, while the directional mode prevails with the thickness below the critical value. The ferroelectricity, including coercive field, remanent polarization, and piezoelectric coefficients, is closely related to the polarization rotation. For example, the energy required for aligning all domains is notably higher in sample 2, considering that +7-V bias induced a single domain in sample 1 with large thickness, while only part of the domain is switched in sample 2 with thin thickness. The coercive field in sample 2 is higher than that in sample 1, considering that the polarization switching is slower and delayed in sample 2 under the same conditions.

It is concluded from the above observation that the 90° ferroelastic domain walls behave as strong barriers for polarization rotation in thin samples. Nevertheless, the tip of domain walls with a unique structural feature (35) leads to different domain switching behaviors under electrical bias. Therefore, it is desired to understand the role of the tip of a domain wall in thin samples. The tip of a domain is unstable (36), where charges accumulate at the tip of a domain, making it easy to initiate domain switching (37). Figure 2 shows snapshot TEM images of an electric biasing process of sample 3, which had the same thickness as sample 2, while having a P_3^-/P_1^- domain configuration with two domain tips ending in the middle of the sample. Domain switching was confined between two domain walls at a bias of −3 V. This confirms that 90° domain walls impede the propagation of domain switching in thin samples. However, when the switched area (marked with green color) reached the domain tip at a bias of −5 V, the P_1^- domain was rapidly converted to P_1^+ domain, expanding the already switched domain area across the domain walls in a very short time. The propagation of domain switching slowed down when another 90° domain wall was confronted (bias, −5 V). Two switched domain areas merged soon after the tip of the domain

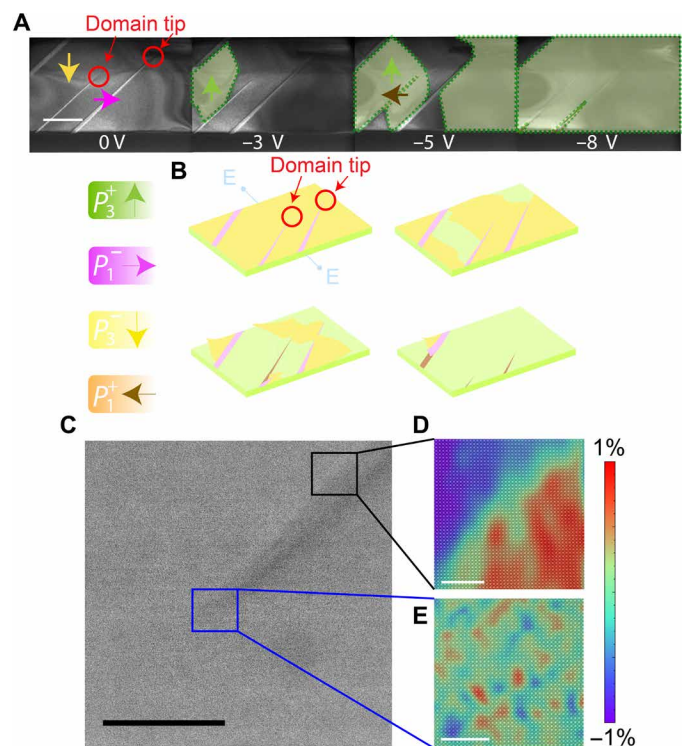


Fig. 2. Role of the tip of a domain wall in domain switching in a thin sample.

(A) A series of images (extracted from movie S3) showing the switching behavior of ferroelectric/ferroelastic domains in a thin sample. The switched domain areas are marked by green/brown colors, while the newly formed domain boundaries are marked by dashed lines. High-resolution HAADF-STEM images were taken for sample 3 before and after biasing to confirm the domain orientation (see section S4 and Materials and Methods for details). Scale bar, 500 nm. (B) Schematic drawing of the domain evolution behavior in (A). Domain evolution exhibits a mixture of the crossing and directional modes due to the existence of domain walls and domain wall tips. (C) A STEM-ABF image showing a domain tip area (scale bar, 20 nm). (D and E) Two STEM-HAADF images overlaid with strain color map (strain tensor ϵ_{xx}) showing the strain areas around the domain tip. Scale bars, 2 nm.

was switched (bias, -8 V). Figure 2B schematically presents the domain switching process. Domain switch followed the directional mode before the tip of the domain was switched. The crossing mode dominated soon after the tip of the domain was switched, where both domains (P_1 and P_3) switched simultaneously, resulting in rapid expansion of the switched domain area. This phenomenon suggests that domain tips weaken the ferroelastic barrier effect of the domains and serve as breaking points to assist ferroelectric/ferroelastic switching in thin samples.

Figure 2C shows a STEM annular bright-field (ABF) image capturing the geometry of the domain tip. Similar to Fig. 1C, large local strain fields existed on both sides of the domain, as shown in Fig. 2D. Of particular importance is that no strain field was found from the area nearby the domain tip, as shown in Fig. 2E, in which less energy is required to trigger domain switching, suggesting the easier domain switching from the domain tip.

DISCUSSION

To understand the thickness effect on domain switching, atomic-resolution HAADF was used to study the microstructure of the sample surface and beneath the surface. A rich variety of structures

and properties were found at the surface of ferroelectric materials (38, 39), which are different from those beneath the surface, especially in thin-film ferroelectrics (25). This is because of the strong lattice mismatch in the film/substrate interface that constrains the depolarization field and therefore controls the polarization configuration on the surface. Although such a lattice constraint caused by a lattice-mismatched interface is not available in single-crystalline ferroelectric materials, the defect and charge accumulation in the amorphous/sample interface can largely affect the surface structure, thus inducing local lattice distortion and surface reconstruction. Figure 3A shows an atomic-resolution HAADF image at the edge of a sample, where it can be observed that a surface region with ~ 30 atomic layers had random polarization. An enlarged interfacial region between the aligned polarization region and the randomly polarized region is shown on the right of Fig. 3A. A large amount of oxygen vacancies are expected to form on the amorphous/sample interface because the asymmetric bonding will lower the formation energy of oxygen vacancies (25). These positively charged defects would migrate to the lattice beneath the surface, thus affecting the depolarization field up to ~ 30 atomic layers.

The reconstructed surface of a single-crystal sample is also reflected by its huge lattice distortion. In perfect crystalline PMN-38%PT structures, the four neighboring Mg/Nb/Ti atoms form a perfect square (nonpolarized) or a rectangle (polarized) lattice (17). However, the atomic-resolution ABF image of a sample surface area in Fig. 3B shows a distorted irregular quadrilateral lattice. Because of the near-surface lattice distortion, a giant local strain region exists in the random polarized region on the proximity of the aligned polarization region. Geometric phase analysis exhibits a huge local strain ($\sim 10\%$) in the random polarized region (Fig. 3C), which is one order of magnitude higher than that measured at 90° ferroelastic domain boundaries (Fig. 1C), revealing the existence of high local strain field area near the ferroelectric surface.

It is well known that 90° ferroelastic domain walls are stressed because of the slight lattice mismatch at the walls between the two neighboring 90° ferroelastic domains. Oxygen vacancies and other defects prefer to accumulate at these domain walls (40, 41). Positive charges exist at domain wall regions near the sample surfaces and internal high-strain domain walls, effectively expanding the local lattice because of the increased Coulomb repulsion between cations. Therefore, an irregular strain region formed at the corner of 90° ferroelastic domain walls and random/aligned polarization interface, as shown in Fig. 3D. Thus, the strained regions in a thin sample will strengthen the pinning of domain walls, substantially restrict the domain wall motion, and slow the domain switching process. The strong strain pinning field between the surface/domain wall was also confirmed by the residual contrast of the domain wall even after the formation of a single domain under the electric field, as shown in Fig. 1D. The strained interface strongly prohibited the complete switching of domains near the interface, leading to a small amount of residual polarization even under strong electrical loading. With increasing the sample thickness, the domain switching process is less affected by the surface/corner strained areas, as it requires less energy for polarization rotation inside the sample. Statistical measurement (details in section S6) showed that the thickness of the reconstructed layer remained almost the same for samples with different thicknesses, suggesting that the ratio of the thicknesses of the reconstructed layer and the whole sample was the major reason that determines the domain switching dynamics.

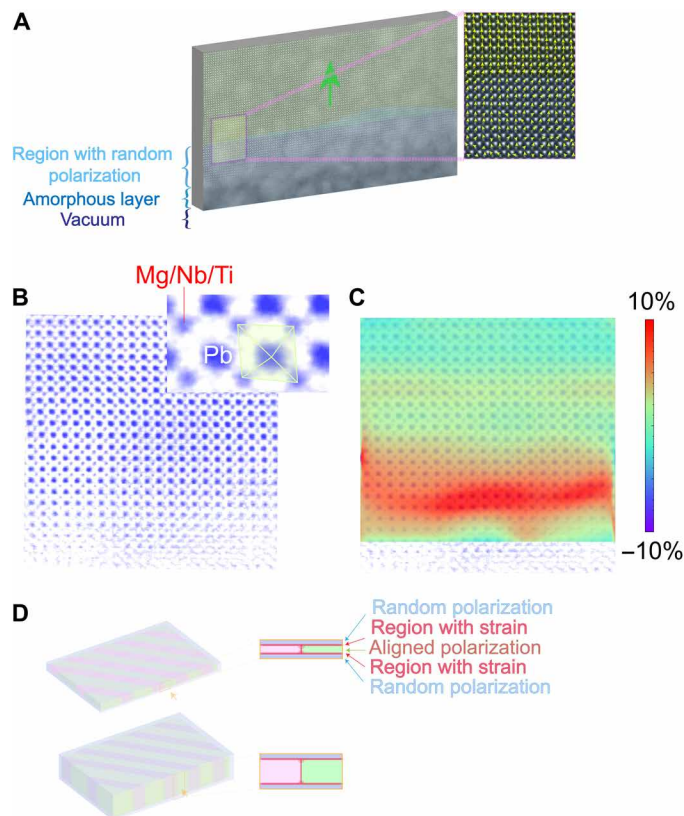


Fig. 3. Origin of the thickness-dependent effect. (A) A high-resolution STEM-HAADF image showing that a randomly polarized region with a thickness of ~30 atomic layers existed in the sample surface layer. The interfacial region of random/aligned polarization is enlarged on the right. (B) A high-resolution STEM-ABF image showing lattice distortion in the sample surface region. The original tetragonal lattice was distorted into an irregular quadrilateral. (C) A STEM-HAADF image overlaid with a strain color map (strain tensor ϵ_{xx}) showing a huge strain field in the ferroelectric surface layer. (D) Schematic drawing showing the effect of strain field on a thick and thin sample. Strain fields (marked with red color) exist in the random/aligned polarization interface and the corner region where ferroelastic domain walls interact with the sample surface. It is obvious that the thick sample is affected less by the surface strain field.

Figure 4A illustrates the schematics of the domain reorganization dynamic for both the crossing mode and the directional mode. Two schematic diagrams with a $P_1^+/P_3^-/P_1^+$ domain configuration for a thick sample (using four atomic columns to represent the thick nature of the sample) and a thin sample (using two atomic columns to represent the thin nature of the sample) are presented. In the thick sample, domain reorganization dynamic presents in the crossing mode. Under the electric field along the [001] direction (the P_3^- direction), three domain reorganization processes take place simultaneously: (i) P_3^- polarization rotates 180° to P_3^+ polarization (green vectors to red vectors), (ii) P_1^+ domains rotate 90° to P_3^+ polarization (blue vectors to red vectors), and (iii) the shrinkage of the P_3^- polarization areas. The energy barrier for 180° and 90° polarization reversals is low in this case, leading to the simultaneous reversal for both 180° and 90° polarizations. The shrinkage of the P_3^- polarization areas has been regularly observed in many thick ferroelectric samples. On the contrary, in the thin sample, domain reorganization occurs via the di-

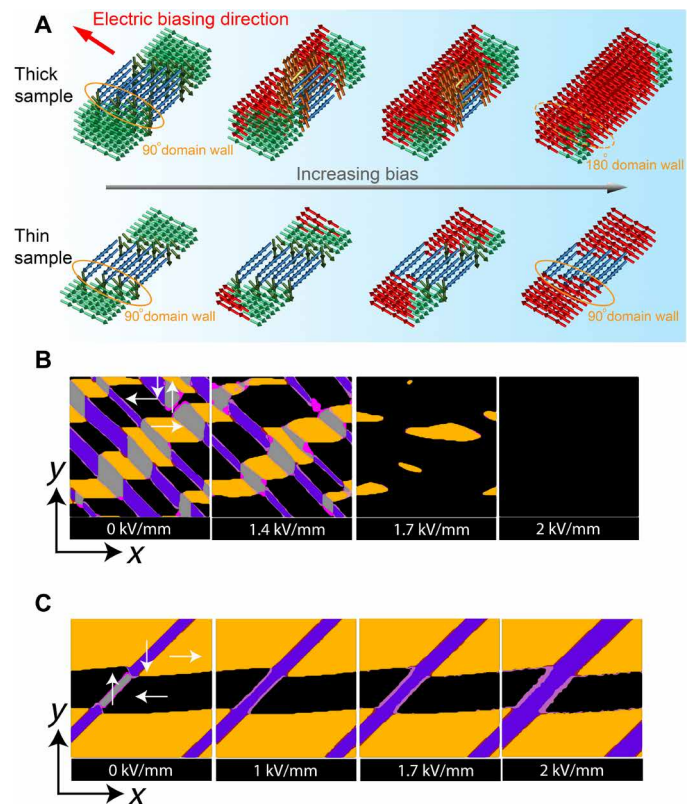


Fig. 4. Phase-field simulation. (A) Schematic illustration of the difference between the crossing mode and directional mode. The 90° and 180° domain walls are marked with orange solid ellipse and dashed ellipse, respectively. (B and C) Phase-field simulations of a thick sample (strain free) and a thin sample (strained). Domain merging into a single domain is found in the strain-free (thick) sample, while domain reversal (switching) along the domain wall direction occurs in the strained (thin) sample.

rectional mode. Under the same electric field direction, only one 180° domain reorientation takes place, in which P_3^- polarization rotates 180° to the P_3^+ polarization (green vectors to red vectors). In this case, because of the sample thickness, the surface reconstruction layers strongly strain the 90° domain wall. The energy barrier for the 90° polarization reversal increased dramatically (see section S5). Because of this strong energy barrier, a charge domain wall P_1^+/P_3^- forms instead of a low-energy-state head-to-tail domain wall. The whole system energy increases greatly under the directional mode compared with the crossing mode, which increases the ferroelectric coercive field dramatically, i.e., makes the polarization rotation harder.

It is understandable that a stand-alone cuboid sample with six surfaces is constrained by the strain field. In an extreme scenario, a thick sample and a thin sample can be considered as a stress-free and a constrained sample, respectively, because of the change of the volume fraction of the strained area to the entire sample. To better understand the observed domain reorganization dynamic processes, phase-field simulations (42, 43) were used to simulate the domain switching dynamics in stress-free and constrained conditions for tetragonal relaxor-PT crystals, as given in Fig. 4 (B and C, respectively). The 90° domain configurations are found in both conditions, confirming the similarity between the initial status of the experimental and simulation results. In the stress-free mode, the domain

switching process shows the typical crossing mode. The switched domains propagate easily and rapidly across domain walls, forming a single domain when sufficiently large bias (along the $-x$ direction) is applied to the sample. As shown in the case when electric field reaches 1.4 kV/mm in the simulation, both 180° and 90° polarization reversals occur in the crossing mode. In contrast, only 180° ferroelectric domain switching occurs (when electric field reaches 1 kV/mm) along the direction of the 90° ferroelastic domain walls under electrical bias (along the $-y$ direction) in the strained mode. No 90° polarization reversal occurs, and no further switching across the domain walls is observed even at higher bias. In the constrained condition, the single domain state is quite difficult to achieve since the switching of ferroelectric domains involves a huge variation of elastic energies under constrained condition when compared with the stress-free condition. The phase-field simulations provide solid evidence, confirming that domain evolutions in samples with different thicknesses follow the constraint or stress-free conditions. The variation of domain switching dynamics due to local strain confinement will directly affect the properties of a ferroelectric, such as the dielectric, piezoelectric, and ferroelectric properties.

In summary, we revealed an unambiguous thickness effect on domain switching dynamic and giant ferroelectricity tailoring in single-crystalline ferroelectrics. For thick samples, switched domains propagate continuously through domain walls. Rapid propagation takes place to align all polarization along the direction of the applied electric field. For thin samples, however, switched domain propagation is much slower and is constrained at domain walls. Substantial strained layers that formed in the random polarized region and the intersection corner of the surface region and 90° ferroelastic domain walls are responsible for the different domain switching dynamics in samples with different thicknesses. The tip of a domain benefits from the lack of strain field nearby, assists the domain switching process, and speeds up the domain evolution even in a thin sample with surface constrained. Phase-field simulations confirm the important role of the reconstructed layer in affecting domain switching behavior. The substantial difference in domain switching dynamics reflects the change of ferroelectricity of single-crystalline ferroelectrics, which provides a potential method to tune ferroelectric properties in nanoscale ferroelectric devices via thickness control.

MATERIALS AND METHODS

Materials synthesis and characterization

The PMN-38%PT single crystal was grown by a modified Bridgman method. In situ TEM samples were prepared using focused ion beam (FIB) milling in a Zeiss Auriga scanning electron microscope. A bulk PMN-38%PT sample was first mechanically polished to a thickness of $\sim 1 \mu\text{m}$ at the edge. Three bars with dimensions of $20 \mu\text{m}$ by $2 \mu\text{m}$ by $1 \mu\text{m}$ was cut from the thin edge of the sample using FIB, was lifted using a tungsten manipulator, and put on a precut copper base. Platinum deposition was used to fix the bar on the Cu base. A thin region was milled from the bar using FIB operated at 30 kV and 50 nA for coarse milling and 10 kV and 10 nA for fine milling. The thickness of the sample is determined by the SEM. TEM observations were carried out using a JEOL JEM-2100 microscope operated at 200 kV. In situ electrical biasing was conducted using a Hysitron PI 95 TEM PicoIndenter with a flat conductive tip. The bias was supplied by a Keithley 2602A SourceMeter integrated in the Electrical Characterization Module. Gentle contact between the con-

ductive tip and the pillar was held for the close-loop electrical loading experiments. The bias was raised from 0 to +10 V (or -10 V) in 40 s (see movies S1 to S3) with a ramping rate of 0.25 V/s (or -0.25 V/s). High-resolution STEM-HAADF images were obtained using a JEOL ARM 200 STEM equipped with a spherical-aberration corrector operated at 200 kV. All STEM images were Fourier filtered using a lattice mask to remove noise. Atomic positions were determined by fitting them as two-dimensional Gaussian peaks using Ranger 2.4 script in MATLAB. Atomic displacement was calculated using MATLAB and presented as the difference vector between the center of a B-site cation and the centers of its four nearest neighboring A-site cations.

Phase-field simulation

The temporal evolution of a polarization field is described by the time-dependent Ginzburg-Landau (TDGL) equation

$$\frac{\partial P_i(\mathbf{r}, t)}{\partial t} = -L \frac{\delta F}{\delta P_i(\mathbf{r}, t)}, \quad (i = 1, 2, 3) \quad (1)$$

where L is the kinetic coefficient, F is the total free energy of the system, and $P_i(\vec{r}, t)$ is the polarization.

The total free energy of the system includes the bulk free energy, elastic energy, electrostatic energy, and the gradient energy

$$F = \int_V [f_{\text{bulk}} + f_{\text{elas}} + f_{\text{elec}} + f_{\text{grad}}] dV \quad (2)$$

where V is the system volume of the polar nano region (PNR)-ferroelectric composite, f_{bulk} denotes the Landau bulk free energy density, f_{elas} denotes the elastic energy density, f_{elec} denotes the electrostatic energy density, and f_{grad} denotes the gradient energy density.

The bulk free energy density is expressed by Landau theory, i.e.

$$\begin{aligned} f_{\text{bulk}} = & \alpha_1(P_1^2 + P_2^2 + P_3^2) + \alpha_{11}(P_1^4 \\ & + P_2^4 + P_3^4) + \alpha_{12}(P_1^2 P_2^2 + P_2^2 P_3^2 \\ & + P_3^2 P_1^2) + \alpha_{111}(P_1^6 + P_2^6 + P_3^6) \\ & + \alpha_{112} [P_1^4(P_2^2 + P_3^2) + P_2^4(P_1^2 + P_3^2) \\ & + P_3^4(P_2^2 + P_1^2)] + \alpha_{123} P_1^2 + P_2^2 + P_3^2 \end{aligned} \quad (3)$$

where α_1 , α_{11} , α_{12} , α_{111} , α_{112} , and α_{123} are Landau energy coefficients. In this work, $\alpha_1 = 2.38(T - 468) \times 10^5 C^{-2} m^2 N$, $\alpha_{11} = 5.56 \times 10^7 C^{-4} m^6 N$, $\alpha_{12} = 3.37 \times 10^8 C^{-4} m^6 N$, $\alpha_{111} = 3.23 \times 10^8 C^{-6} m^{10} N$, $\alpha_{112} = 1.02 \times 10^9 C^{-6} m^{10} N$, and $\alpha_{123} = 1.21 \times 10^9 C^{-6} m^{10} N$. These parameters are referred from the data of PZN-0.15%PT crystals (44), whose phase and domain structures are similar to that of PMN-38%PT.

The gradient energy density, associated with the formation and evolution of domain walls, can be expressed as

$$\begin{aligned} f_{\text{grad}} = & \frac{1}{2} G_{11}(P_{1,1}^2 + P_{2,2}^2 + P_{3,3}^2) + G_{12}(P_{1,1} P_{2,2} + P_{2,2} P_{3,3} + P_{1,1} P_{3,3}) \\ & + \frac{1}{2} G_{44} [(P_{1,2} P_{2,1})^2 + (P_{2,3} P_{3,2})^2 + (P_{1,3} P_{3,1})^2] \\ & + \frac{1}{2} G'_{44} [(P_{1,2} P_{2,1})^2 + (P_{2,3} P_{3,2})^2 + (P_{1,3} P_{3,1})^2] \end{aligned} \quad (4)$$

where G_{ij} are gradient energy coefficients. $P_{i,j}$ denote $\partial P_i / \partial r_j$.

The corresponding elastic energy density can be expressed as

$$f_{\text{elas}} = \frac{1}{2} c_{ijkl} e_{ij} e_{kl} = \frac{1}{2} c_{ijkl} (\epsilon_{ij} - \epsilon_{ij}^0) (\epsilon_{kl} - \epsilon_{kl}^0) \quad (5)$$

where c_{ijkl} is the elastic stiffness tensor, ϵ_{ij} is the total strain, ϵ_{kl}^0 is the electrostrictive stress-free strain, i.e., $\epsilon_{kl}^0 = Q_{ijkl} P_k P_l$.

The electrostatic energy density is given by

$$f_{\text{elec}} = -\frac{1}{2} E_i^{\text{in}} P_i - E_i^{\text{ex}} P_i \quad (6)$$

where E_i^{in} is the electric field induced by the dipole moments in the sample. E_i^{ex} is an applied external electric field.

A semi-implicit Fourier spectral method is adopted for numerically solving the TDGL equation (43). The elastic constants and electrostrictive coefficients are set to be $s_{11}^D = 20 \times 10^{-12} \text{ m}^2/\text{N}$, $s_{12}^D = -7.5 \times 10^{-12} \text{ m}^2/\text{N}$, $s_{44}^D = 20 \times 10^{-12} \text{ m}^2/\text{N}$, $Q_{11} = 0.089 \text{ C}^{-2} \text{ m}^4$, $Q_{12} = 0.030 \text{ C}^{-2} \text{ m}^4$, and $Q_{44} = 0.034 \text{ C}^{-2} \text{ m}^4$. The background dielectric permittivity (k_b), associated with the contribution of the hard mode to the permittivity, is set to be $100 \times \epsilon_0$. In the computer simulations, we used 2D 128×128 discrete grid points and periodic boundary conditions. The grid space in real space is chosen to be $\Delta x = \Delta y = 1 \text{ nm}$. The gradient energy coefficients are chosen to be $G_{11}/G_{110} = 1.5$, $G_{12}/G_{110} = 0$, and $G_{44}/G_{110} = G_{44}/G_{110} = 0.75$, where $G_{110} = 7.04 \times 10^{-11} \text{ C}^{-2} \text{ m}^4 \text{ N}$. On the basis of these parameters, the simulated width of domain walls was found to be 1 to 2 nm, which is consistent with existing experimental measurements.

In the simulations, we used a periodic boundary condition for phase-field modeling. For the stress-free condition, the surface stress is zero. For the constrained condition, the total strain is not changed so that the presence of surface stresses is to prevent the strain variation. The constrained strain condition means that the average (homogeneous) strains of the system (e_1, e_2, e_3, e_4, e_5 , and e_6) are zero during the application of electric field. This means that the surface tension is positive if the surface is inclined to shrink, while it is negative if the surface is inclined to extend.

SUPPLEMENTARY MATERIALS

Supplementary material for this article is available at <http://advances.sciencemag.org/cgi/content/full/6/42/eabc7156/DC1>

REFERENCES AND NOTES

- J. Kuwata, K. Uchino, S. Nomura, Dielectric and piezoelectric properties of $0.91\text{Pb}(\text{Zn}_{1/3}\text{Nb}_{2/3})\text{O}_3$ - 0.09PbTiO_3 single crystals. *Jpn. J. Appl. Phys.* **21**, 1298–1302 (1982).
- S.-E. Park, T. R. Shrout, Ultrahigh strain and piezoelectric behavior in relaxor based ferroelectric single crystals. *J. Appl. Phys.* **82**, 1804–1811 (1997).
- F. Li, D. Lin, Z. Chen, Z. Cheng, J. Wang, C. C. Li, Z. Xu, Q. Huang, X. Liao, L.-Q. Chen, T. R. Shrout, S. Zhang, Ultrahigh piezoelectricity in ferroelectric ceramics by design. *Nat. Mater.* **17**, 349–354 (2018).
- Z. Chen, X. Wang, S. Ringer, X. Liao, Manipulation of nanoscale domain switching using an electron beam with omnidirectional electric field distribution. *Phys. Rev. Lett.* **117**, 027601 (2016).
- Z. Chen, L. Hong, F. Wang, X. An, X. Wang, S. Ringer, L.-Q. Chen, H. Luo, X. Liao, Kinetics of domain switching by mechanical and electrical stimulation in relaxor-based ferroelectrics. *Phys. Rev. Appl.* **8**, 064005 (2017).
- S. Zhang, F. Li, X. Jiang, J. Kim, J. Luo, X. Geng, Advantages and challenges of relaxor-PbTiO₃ ferroelectric crystals for electroacoustic transducers—A review. *Prog. Mater. Sci.* **68**, 1–66 (2015).
- K. K. Shung, M. Zippuro, Ultrasonic transducers and arrays. *IEEE Eng. Med. Biol. Mag.* **15**, 20–30 (1996).

- J. M. Cannata, J. A. Williams, Z. Qifa, T. A. Ritter, K. K. Shung, Development of a 35-MHz piezo-composite ultrasound array for medical imaging. *IEEE Trans. Ultrason. Ferroelectr. Freq. Control* **53**, 224–236 (2006).
- Y. Huang, Y. Xia, D. H. Lin, K. Yao, L. C. Lim, Large stroke high fidelity PZn-PT single-crystal “Stake” actuator. *IEEE Trans. Ultrason. Ferroelectr. Freq. Control* **64**, 1617–1624 (2017).
- S. Zhang, F. Li, High performance ferroelectric relaxor-PbTiO₃ single crystals: Status and perspective. *J. Appl. Phys.* **111**, 031301 (2012).
- Z. Liu, T. Lu, J. Ye, G. Wang, X. Dong, R. Withers, Y. Liu, Antiferroelectrics for energy storage applications: A review. *Adv. Mater. Technol.* **3**, 1800111 (2018).
- E. Sun, W. Cao, Relaxor-based ferroelectric single crystals: Growth, domain engineering, characterization and applications. *Prog. Mater. Sci.* **65**, 124–210 (2014).
- F. Li, S. Zhang, Z. Xu, L. Q. Chen, The contributions of polar nanoregions to the dielectric and piezoelectric responses in domain-engineered relaxor-PbTiO₃ crystals. *Adv. Funct. Mater.* **27**, 1700310 (2017).
- F. Li, M. J. Cabral, B. Xu, Z. Cheng, E. C. Dickey, J. M. Le Beau, J. Wang, J. Luo, S. Taylor, W. Hackenberger, L. Bellaiche, Z. Xu, L.-Q. Chen, T. R. Shrout, S. Zhang, Giant piezoelectricity of Sm-doped $\text{Pb}(\text{Mg}_{1/3}\text{Nb}_{2/3})\text{O}_3$ -PbTiO₃ single crystals. *Science* **364**, 264–268 (2019).
- R. G. P. McQuaid, L.-W. Chang, J. M. Gregg, The effect of antinotches on domain wall mobility in single crystal ferroelectric nanowires. *Nano Lett.* **10**, 3566–3571 (2010).
- P. Sharma, R. G. P. McQuaid, L. J. McGilly, J. M. Gregg, A. Gruverman, Nanoscale dynamics of superdomain boundaries in single-crystal BaTiO₃ lamellae. *Adv. Mater.* **25**, 1323–1330 (2013).
- Z. Chen, L. Hong, F. Wang, S. P. Ringer, L.-Q. Chen, H. Luo, X. Liao, Facilitation of ferroelectric switching via mechanical manipulation of hierarchical nanoscale domain structures. *Phys. Rev. Lett.* **118**, 017601 (2016).
- S. Zhang, Y. Zhu, Y. Tang, Y. Liu, S. Li, M. Han, J. Ma, B. Wu, Z. Chen, S. Saremi, X. Ma, Giant polarization sustainability in ultrathin ferroelectric films stabilized by charge transfer. *Adv. Mater.* **29**, 1703543 (2017).
- P. Gao, Z. Zhang, M. Li, R. Ishikawa, B. Feng, H.-J. Liu, Y.-L. Huang, N. Shibata, X. Ma, S. Chen, J. Zhang, K. Liu, E.-G. Wang, D. Yu, L. Liao, Y.-H. Chu, Y. Ikuhara, Possible absence of critical thickness and size effect in ultrathin perovskite ferroelectric films. *Nat. Commun.* **8**, 15549 (2017).
- T. M. Shaw, S. Trolier-McKinstry, P. C. McIntyre, The properties of ferroelectric films at small dimensions. *Annu. Rev. Mater. Sci.* **30**, 263–298 (2000).
- M. P. Cruz, Y. H. Chu, J. X. Zhang, P. L. Yang, F. Zavaliche, Q. He, P. Shafer, L. Q. Chen, R. Ramesh, Strain control of domain-wall stability in epitaxial BiFeO₃ (110) films. *Phys. Rev. Lett.* **99**, 217601 (2007).
- T. Matsushima, I. Kanno, K. Wasa, in *Handbook of Sputtering Technology*, K. Wasa, I. Kanno, H. Kotera, Eds. (William Andrew Publishing, ed. 2, 2012), pp. 559–596.
- A. Bernal, A. Tselev, S. Kalinin, N. Bassiri-Gharb, Free-standing ferroelectric nanotubes processed via soft-template infiltration. *Adv. Mater.* **24**, 1160–1165 (2012).
- G. Catalan, J. Seidel, R. Ramesh, J. F. Scott, Domain wall nanoelectronics. *Rev. Mod. Phys.* **84**, 119–156 (2012).
- P. Gao, H.-J. Liu, Y.-L. Huang, Y.-H. Chu, R. Ishikawa, B. Feng, Y. Jiang, N. Shibata, E.-G. Wang, Y. Ikuhara, Atomic mechanism of polarization-controlled surface reconstruction in ferroelectric thin films. *Nat. Commun.* **7**, 11318 (2016).
- M. H. Park, Y. H. Lee, H. J. Kim, T. Schenk, W. Lee, K. D. Kim, F. P. G. Fengler, T. Mikolajick, U. Schroeder, C. S. Hwang, Surface and grain boundary energy as the key enabler of ferroelectricity in nanoscale hafnia-zirconia: A comparison of model and experiment. *Nanoscale* **9**, 9973–9986 (2017).
- Y. M. Jin, Y. U. Wang, A. G. Khachatryan, J. F. Li, D. Viehland, Conformal miniaturization of domains with low domain-wall energy: Monoclinic ferroelectric states near the morphotropic phase boundaries. *Phys. Rev. Lett.* **91**, 197601 (2003).
- Y.-H. Shin, I. Grinberg, I.-W. Chen, A. M. Rappe, Nucleation and growth mechanism of ferroelectric domain-wall motion. *Nature* **449**, 881–884 (2007).
- F. Chu, I. M. Reaney, N. Setter, Role of defects in the ferroelectric relaxer lead scandium tantalate. *J. Am. Ceram. Soc.* **78**, 1947–1952 (1995).
- A. Pramanick, A. D. Prewitt, J. S. Forrester, J. L. Jones, Domains, domain walls and defects in perovskite ferroelectric oxides: A review of present understanding and recent contributions. *Crit. Rev. Solid State Mater. Sci.* **37**, 243–275 (2012).
- K. Garrity, A. M. Kolpak, S. Ismail-Beigi, E. I. Altman, Chemistry of ferroelectric surfaces. *Adv. Mater.* **22**, 2969–2973 (2010).
- P. Potnis, J. Huber, In-situ observation of needle domain evolution in barium titanate single crystals. *J. Eur. Ceram. Soc.* **33**, 327–333 (2013).
- Y. Sato, T. Hirayama, Y. Ikuhara, Evolution of nanodomains under DC electrical bias in $\text{Pb}(\text{Mg}_{1/3}\text{Nb}_{2/3})\text{O}_3$ -PbTiO₃: An in-situ transmission electron microscopy study. *Appl. Phys. Lett.* **100**, 172902 (2012).
- Z. Chen, Q. Huang, F. Wang, S. P. Ringer, H. Luo, X. Liao, Stress-induced reversible and irreversible ferroelectric domain switching. *Appl. Phys. Lett.* **112**, 152901 (2018).
- P. Gao, J. Britson, C. T. Nelson, J. R. Jokisaari, C. Duan, M. Trassin, S.-H. Baek, H. Guo, L. Li, Y. Wang, Y.-H. Chu, A. M. Minor, C.-B. Eom, R. Ramesh, L.-Q. Chen, X. Pan, Ferroelastic

- domain switching dynamics under electrical and mechanical excitations. *Nat. Commun.* **5**, 3801 (2014).
36. B. Jiang, Y. Bai, W. Chu, Y. Su, L. Qiao, Direct observation of two 90° steps of 180° domain switching in BaTiO₃ single crystal under an antiparallel electric field. *Appl. Phys. Lett.* **93**, 152905 (2008).
 37. P. S. Bednyakov, T. Sluka, A. K. Tagantsev, D. Damjanovic, N. Setter, Formation of charged ferroelectric domain walls with controlled periodicity. *Sci. Rep.* **5**, 15819 (2015).
 38. D. D. Fong, A. M. Kolpak, J. A. Eastman, S. K. Streiffer, P. H. Fuoss, G. B. Stephenson, C. Thompson, D. M. Kim, K. J. Choi, C. B. Eom, I. Grinberg, A. M. Rappe, Stabilization of monodomain polarization in ultrathin PbTiO₃ films. *Phys. Rev. Lett.* **96**, 127601 (2006).
 39. A. G. Zembilgotov, N. A. Pertsev, H. Kohlstedt, R. Waser, Ultrathin epitaxial ferroelectric films grown on compressive substrates: Competition between the surface and strain effects. *J. Appl. Phys.* **91**, 2247–2254 (2002).
 40. Y. Du, X. Wang, D. Chen, Y. Yu, W. Hao, Z. Cheng, S. X. Dou, Manipulation of domain wall mobility by oxygen vacancy ordering in multiferroic YMnO₃. *Phys. Chem. Chem. Phys.* **15**, 20010–20015 (2013).
 41. W. Li, A. Chen, X. Lu, J. Zhu, Collective domain-wall pinning of oxygen vacancies in bismuth titanate ceramics. *J. Appl. Phys.* **98**, 024109 (2005).
 42. L.-Q. Chen, Phase-field method of phase transitions/domain structures in ferroelectric thin films: A review. *J. Am. Ceram. Soc.* **91**, 1835–1844 (2008).
 43. L.-Q. Chen, Phase-field models for microstructure evolution. *Annu. Rev. Mat. Res.* **32**, 113–140 (2002).
 44. F. Li, S. Zhang, T. Yang, Z. Xu, N. Zhang, G. Liu, J. Wang, J. Wang, Z. Cheng, Z.-G. Ye, J. Luo, T. R. Shrout, L.-Q. Chen, The origin of ultrahigh piezoelectricity in relaxor-ferroelectric solid solution crystals. *Nat. Commun.* **7**, 13807 (2016).

Acknowledgments: We are grateful for the scientific and technical support from the Microscopy Australia node at the University of Sydney (Sydney Microscopy & Microanalysis)

and the assistance of D. Mitchell of the Electron Microscopy Centre of the University of Wollongong. **Funding:** This research was financially supported by the Australian Research Council (DP190101155). S.Z. thanks the support of ARC (FT140100698) and ONRG (N62909-18-12168). F. Li acknowledges the support of the National Natural Science Foundation of China (grant nos. 51922083 and 51831010) and the 111 Project (B14040). The work at Penn State is supported by the U.S. NSF under grant no. DMR-1744213. F.W. acknowledges the support of the National Natural Science Foundation of China (grant no. 11974250) and the Science and Technology Commission of Shanghai Municipality (grant no. 19070502800). H.L. acknowledges the key project of the National Natural Science Foundation of China (no. 51831010) and the key program of the Fujian Institute of Innovation, CAS (no. FJCY18040205). **Authors contributions:** Z.C. and X.L. designed and directed the study. Z.C. conducted the microscopy experiments and performed data analysis. Q.H. assisted in the experiment. F. Liu and F.W. provided the samples and performed measurement in bulk samples. F. Li conducted phase-field modeling. Z.C., F. Li, S.P.R., S.Z., L.-Q.C., and X.L. wrote the paper. All authors discussed the results and contributed to the paper. All authors read and approved the final manuscript. **Competing interests:** The authors declare that they have no competing interests. **Data and materials availability:** All data needed to evaluate the conclusions in the paper are present in the paper and/or the Supplementary Materials. Additional data related to this paper may be requested from the authors.

Submitted 11 May 2020

Accepted 28 August 2020

Published 14 October 2020

10.1126/sciadv.abc7156

Citation: Z. Chen, F. Li, Q. Huang, F. Liu, F. Wang, S. P. Ringer, H. Luo, S. Zhang, L.-Q. Chen, X. Liao, Giant tuning of ferroelectricity in single crystals by thickness engineering. *Sci. Adv.* **6**, eabc7156 (2020).